



Higher-order organization of multivariate time series

In the format provided by the
authors and unedited

Supplementary Material: Higher-order organization of multivariate time series

Andrea Santoro*, Federico Battiston[†], Giovanni Petri[○], Enrico Amico^{*,‡}

^{*}Neuro-X Institute, École Polytechnique Fédérale de Lausanne, Geneva, 1202, Switzerland

[†]Department of Network and Data Science, Central European University, Vienna, 1100, Austria

[○]CENTAI, Corso Re Inghilterra 3, Turin, 10138, Italy

[‡]Department of Radiology and Medical Informatics, University of Geneva, Geneva, 1211, Switzerland

Contents

S1 Filtration and persistent homology	2
S2 Global behaviour of Coupled Map Lattice (CML)	4
S2.1 Effect of z -scores and signs assignment in CML time series	4
S3 Comparison of time series approaches to distinguish the CML regimes	6
S4 Impact of different null models	9
S4.1 CML synthetic multivariate time series	9
S4.2 Block null model in financial time series	12
S4.3 Null model of fMRI time series and Gaussian hypothesis	13
S5 Edge-based indicators in real-world systems	14
S6 Local higher-order indicators in real-world systems	18
S6.1 Role of thresholds in brain maps	18
S6.2 Higher-order indicators in the brain's functional networks	18
S7 Additional real-world application: the US historical data of infectious diseases	20
S7.1 Comparison of classifiers for the US historical data	20
S8 Impact of 3D-cavities in CML	22
S9 Effect of noisy fluctuations in brain data	23

S1 Filtration and persistent homology

In the main text, we introduced the simplicial filtration $\mathbb{F}(\mathcal{K}^t)$ as one of the main steps of our higher-order framework. More precisely, for each time t , this object represents a sequence of embedded simplicial complexes, sorted according to coherent patterns, starting with the empty complex and ending with the entire simplicial complex \mathcal{K}^t , i.e. $\emptyset = \mathcal{S}_0 \subset \mathcal{S}_1 \subset \dots \subset \mathcal{S}_t \subset \dots \subset \mathcal{S}_n \subset \mathcal{K}^t$. We then considered the persistent homology of \mathbb{F} to characterize the persistency of 1D cycles in the filtration, i.e. the persistent generators of the first homology group H_1 , which provide insights about where and when higher synchronised regions emerge.

In Fig. S1 we report a schematic representation of the persistent homology computation and the corresponding definition of the hyper-complexity contributes considered in this work. In particular, Fig. S1a reports an illustrative example of a simplicial filtration in two-dimensions. The outputs of persistent homology are barcodes, which represent a compressed description of the homological features of a space (see Fig. S1b). Each bar corresponds to a specific topological feature, which can be identified in terms of a “time-stamp” recording the birth w_b and death w_d of that feature along the filtration. In the main text, we characterized the evolution of 1D cycles along such a filtration — the blue bars in Fig. S1b — by relying on persistence diagrams, which provide an equivalent description of bar codes. In this 2-dimensional plot, each 1D cycle is represented by a point with coordinates (w_b, w_d) (see Fig. S1c).

Furthermore, we defined the *hyper-complexity indicator* as the Wasserstein distance [1] between the persistence diagram of H_1 and the empty persistence diagram, corresponding to a space with trivial H_1 homology. However, to better characterize the evolution of 1D cycles in the space of coherent and decoherent co-fluctuations, we decompose the hyper-complexity indicator into three different contributions. That is, as we track the evolution of 1D cycles along the filtration, we focus on 1D cycles that are created and closed only by fully coherent structures, i.e. edges and triangles having a weight larger than zero, which we renamed as a Full Coherence (FC) contribution; 1D cycles formed by coherent structures and closed by the decoherent ones (i.e. edges and triangles with a weight smaller than zero), which we renamed as a Coherence Transition (CT) contribution; 1D cycles created only by the fully decoherent structures, renamed as a Full Decoherence (FD) contribution.

In Fig. S1d, the three fractional contributions of the hyper-complexity indicator are reported in a triangular representation.

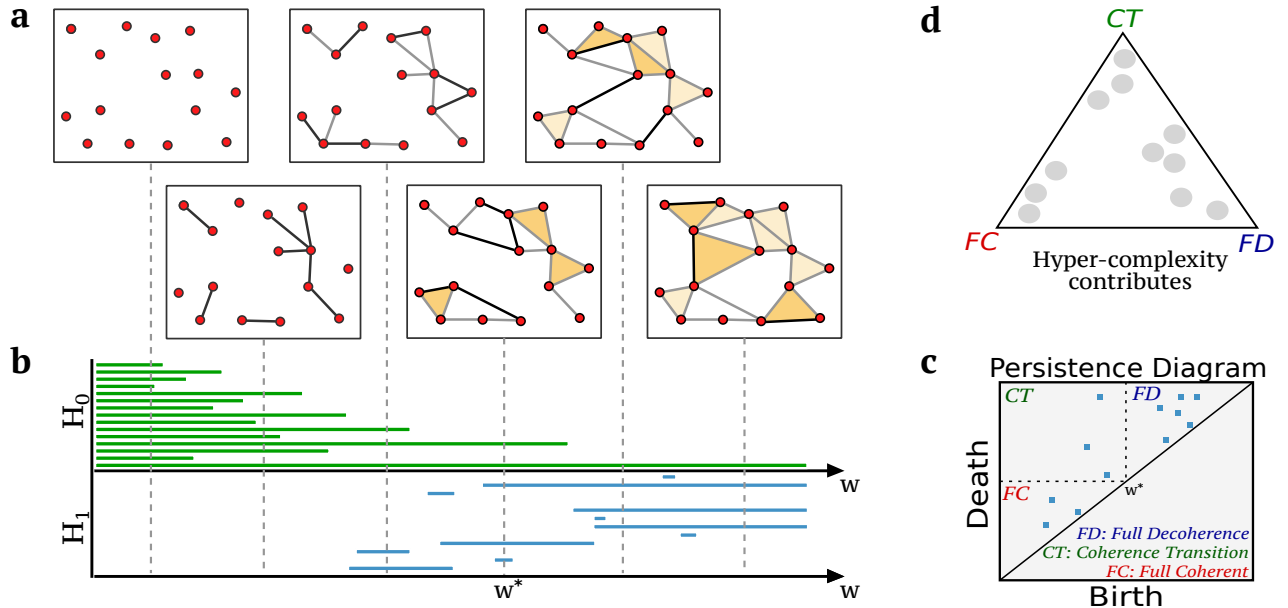


Figure S1: Pictorial representation of persistent homology computation and definition of hyper-complexity contributes. (a) Example of a simplicial filtration in two-dimensions. (b) Barcodes describe the lifetime of different topological features across multiple scales. Here, green bars identify the persistence of various connected components (describing H_0), progressively merging into each other until only one survives, whereas blue bars describe the lifetime of 1-dimensional cycles (describing H_1). Hence, each bar corresponds to a specific topological feature, which can be identified in terms of a “time-stamp” recording the birth w_b and death w_d of that feature along the filtration. (c) Persistence diagrams provide an equivalent description of barcodes. For example, if we focus only on H_1 , each 1D cycle is represented in the 2-dimensional plot by a point with coordinates (w_b, w_d) . In this work, we further distinguish the nature of 1D cycles depending on the corresponding time-stamps, i.e. whether 1D cycles are created and closed before/after $w^* = 0$, therefore reflecting pure coherent (resp. incoherent) structures. (d) The hyper-complexity indicator, defined as the Wasserstein distance [1] between the persistence diagram of H_1 and the empty persistence diagram, can be then decomposed into three different contributes according to the nature of 1D cycles and, for each time t , such contributes can be plotted in a triangular representation.

S2 Global behaviour of Coupled Map Lattice (CML)

In the main text, we considered $N = 119$ diffusively coupled fully chaotic maps to generate synthetic multivariate time series with different dynamical regimes. CMLs are widely used to model complex spatiotemporal dynamics in several different fields including biology [2], and finance [3, 4]. In Fig. S2a we report a sample of such time series in three different lattice sites, showing the general behaviour of the five different dynamical states. Moreover, the space-amplitude plot [5, 6] reported in Fig. S2b, which depicts the temporal evolution of $x_i(t)$ at each lattice site i , clearly shows the overall behaviour of the five dynamical regimes.

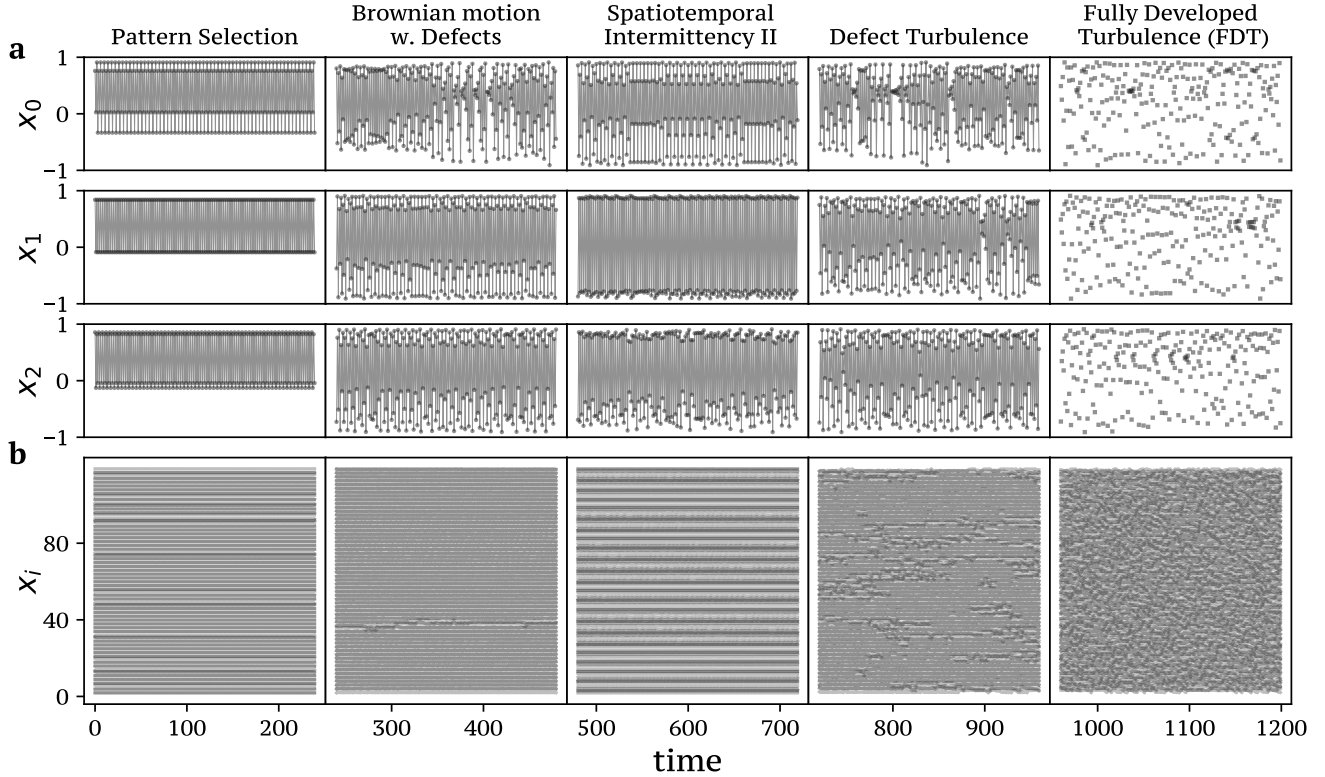


Figure S2: Sample of the coupled map lattice (a) We report a sample of the time series considered in the main text and generated by $N = 119$ diffusively coupled fully chaotic maps at different values of the coupling strength ε . Namely, from ordered to disordered systems: Pattern Selection (PS) at $\varepsilon = 0.12$, Brownian motion with Defects (BMWD) at $\varepsilon = 0.08$, Spatiotemporal Intermittency II (STI) at $\varepsilon = 0.3$, Defect Turbulence (DT) at $\varepsilon = 0.068$, and Fully Developed Turbulence (FDT) at $\varepsilon = 0.05$, for which a transient of 10^5 time points has been removed. (b) The space-amplitude plot, reporting the temporal evolution of $x_i(t)$ at each lattice site i , clearly reflects the different global behaviour of the five dynamical regimes.

S2.1 Effect of z -scores and signs assignment in CML time series

In one of the main steps of the simplicial framework described in the main text, we rely on the z -score for each group product time series to allow comparison across k -orders and to create proper simplicial filtrations. After that, a choice on how to assign signs to the resulting weights is required in order to distinguish fully concordant group interactions (all positive or negative fluctuations) from discordant

ones (a mixture of positive and negative fluctuations) in a k -order product. In order to distinguish fully concordant group interactions (all positive or negative fluctuations) from discordant ones (a mixture of positive and negative fluctuations) in a k -order product, we assign positive signs to the fully concordant group interactions, and negative signs to the discordant ones. However, this way of assigning signs means that the baseline score might be slightly altered and, as a result, the concordance might be harder to achieve for a triangle than for an edge.

In Figure S3, we analyse the impact of z -score and signs assignment in edges and triangles distributions for the coupled map lattice dynamical states. In particular, the z -scores and signs assignment for triangles produce a negative offset with respect to that of edges. This phenomenon does not have a deep impact in the hyper-coherence indicator, since it is defined as the fraction of violating coherent triangles (i.e. violating triangles with a weight greater than zero) over all the possible coherent triangles (i.e. triangles with a weight greater than zero). By contrast, the negative offset of the triangle weight distribution over the edges one might have an impact in the hyper-complexity indicator. This is due to the fact that this indicator is constructed by considering the ensemble of both edges and triangles weight distribution. However, the effect on hyper-complexity is a shift in the contributions from the fully coherent to the other two contributions, rather than a restructuring of the whole simplicial filtration. In this sense, the effect is a biasing one.

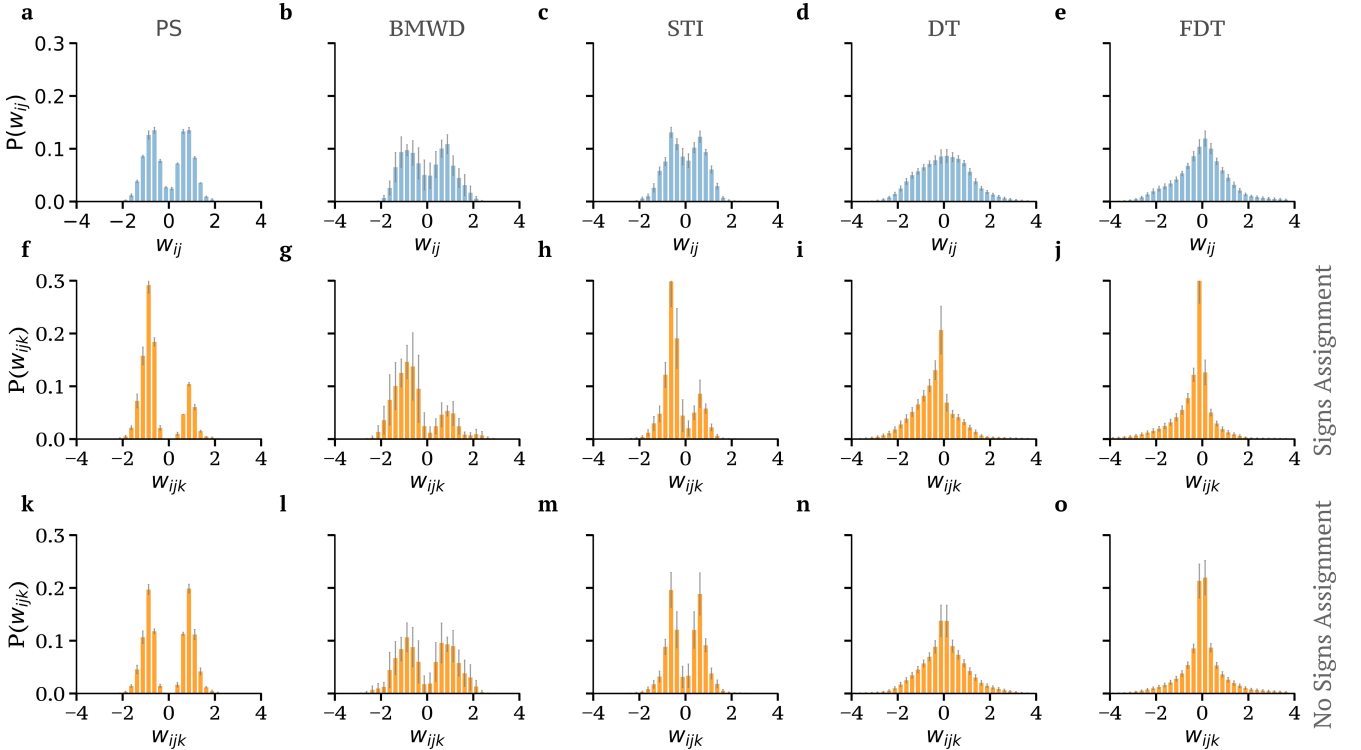


Figure S3: Impact of z -score and signs assignment in edge and triangles distributions for the coupled map lattice. For each of the five CML dynamical states, we report the distribution of weights of edges (a-e) and triangles with (f-j) and without the sign assignment (k-o), respectively. Notice that the z -scores and signs assignment produce a negative offset for triangles with respect to that of edges. While this phenomenon does not have a deep impact in the hyper-coherence indicator for the way such a measure is constructed, the hyper-complexity indicator might be shifted by such offset. It is also worth remarking that when sign remapping is not performed, it is not possible to identify a triangle with a synchronous co-activation pattern from its weight, given that decoherent triangles might end up having the same weights as fully coherent ones. Error bars represent standard deviations over 240 time points.

S3 Comparison of time series approaches to distinguish the CML regimes

In this section, we provide a detailed investigation of the ability of different indicators to differentiate the five regimes generated by $N = 119$ diffusively coupled fully chaotic maps, extensively considered in the main text. The multivariate time series consists of $N = 119$ nodes and $T = 1200$, obtained by concatenating five different CML regimes with fixed time length $L = 240$.

We first compare our higher-order measures with the lower-order dynamical indicator originally proposed in Ref. [7]. This is the Root Sum Square (RSS) of the edge-time series, which was recently used to identify important “events” in fMRI signals [7, 8], and it is a direct proxy of the amplitude of the collective co-fluctuations of the edge time series. In other words, we compute the amplitude of the edge time series as the root sum of squared co-fluctuations, i.e. $RSS(t) = \sqrt{\sum_{i,j>i} e_{ij}(t)^2}$. Here, the vector $\mathbf{e}_{ij} = \mathbf{z}_i \mathbf{z}_j$ is the edge time series obtained as a product of the z -scores of the original time series. We then assess the performance of several other “static” approaches, namely, (i) the information-theoretic approaches introduced in Refs. [9, 10] accounting for higher-order interactions, (ii) the dyadic method at the interface of network science and random matrix theory [11], and (iii) the classical approach based on Pearson’s correlation coefficient [12].

Top panels of Figure S4 depict the violin plots of the distribution of RSS and of the three higher-order measures for the five regimes of the CMLs. Surprisingly, the RSS distributions of certain dynamical

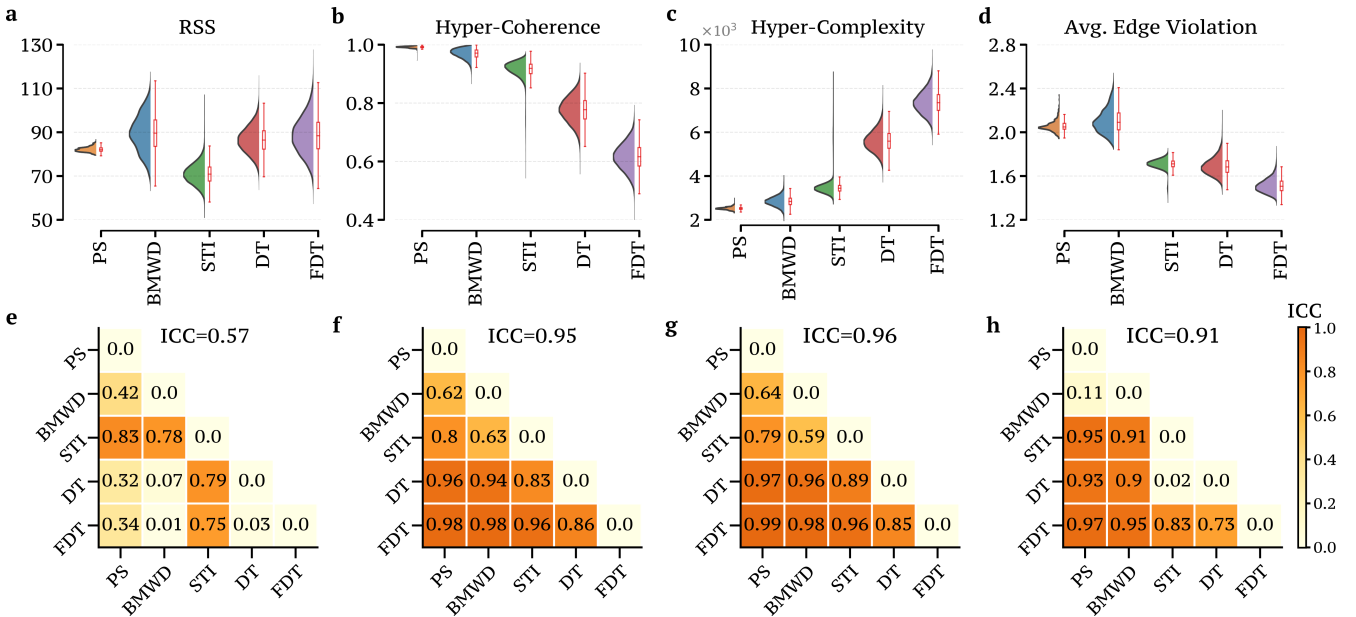


Figure S4: Comparison of different dynamical metrics. (a-d) Violin plots showing the distribution of RSS (Root Sum Square) and three higher-order measures for the five different dynamical regimes generated by the diffusively coupled chaotic maps. Remarkably, the RSS statistic, which only captures the effect of lower-order structures (i.e. the edges), is not able to well-separate the five dynamical regimes. By contrast, the higher-order metrics introduced in this work distinguish the different regimes. (e-h) The performance of each indicator is quantitatively measured by the ICC values computed either considering the five distributions or between all the possible pairs. When considering all the five distributions, we find RSS with an $ICC \approx 0.57$, hyper-coherence with $ICC \approx 0.95$, hyper-complexity with $ICC \approx 0.96$, and average edge violation with $ICC \approx 0.91$. Results are averaged over 100 independent realizations.

states (BMWD, DT, and FDT) are highly similar to each other, somehow mirroring the inability to capture the subtleties of these regimes. By contrast, the higher-order measures seem to differentiate the dynamical states in a qualitatively better way. As a matter of fact, the ability to distinguish the different dynamical regimes is quantitatively confirmed by the *ICC* values [13, 14] associated with each metric and reported in the bottom panels. In particular, we have RSS with an $ICC \approx 0.57$, hyper-coherence with $ICC \approx 0.95$, hyper-complexity with $ICC \approx 0.96$, and average edge violation with $ICC \approx 0.91$. For the sake of completeness, for each dynamical measure we also report an ICC matrix encoding the ICC values between all the possible pairwise comparison of dynamical regimes. Moreover, it is also interesting to notice how the five CML regimes map onto distinct hyper-coherence distributions mirroring peculiar features intrinsic to each spatiotemporal regime. For instance, apart from a well-defined bulk, the STI regime exhibits a long tail towards lower hyper-coherence values, which captures the rare appearance of short chaotic bursts arising from the mismatching of the dynamical phases [5, 15, 16].

Lastly, for each of the five CML regimes, we independently compute diverse “static” higher-order and pairwise measures [12, 11, 9, 10], aggregating the results across 100 independent realizations. In other words, after isolating each dynamical state by selecting the precise intervals of size $T = 240$, we compute the selected measure on that interval. This is necessary, since such measures are not dynamic (i.e. they are not defined on a single frame), but instead they require a time-window to be computed.

Figure S5 reports the results of our analyses for the different approaches. Remarkably, several of the information-theoretic measures introduced by Rosas and colleagues [9] [see Figs. S5(a-d)] are able to differentiate in a quantitative way the different CML dynamical states, as confirmed by the high ICC values reported in panels S5(g-j)¹. By contrast, approaches only based on pairwise statistical dependencies [see Figs. S5(e-f)], such as “connectome” analyses based on Pearson’s correlation ρ or the filtered ρ relying on random matrix theory [11], fail at differentiating the five dynamical regimes [see Figs. S5(k-l)]. To confirm the quantitative analyses provided by the ICC metric, we repeat an analogous analysis but considering the Jensen-Shannon (JS) divergence to measure distances between distributions [see Figs. S5(m-r)].

¹The code for these analyses has been adapted from Ref. [10].

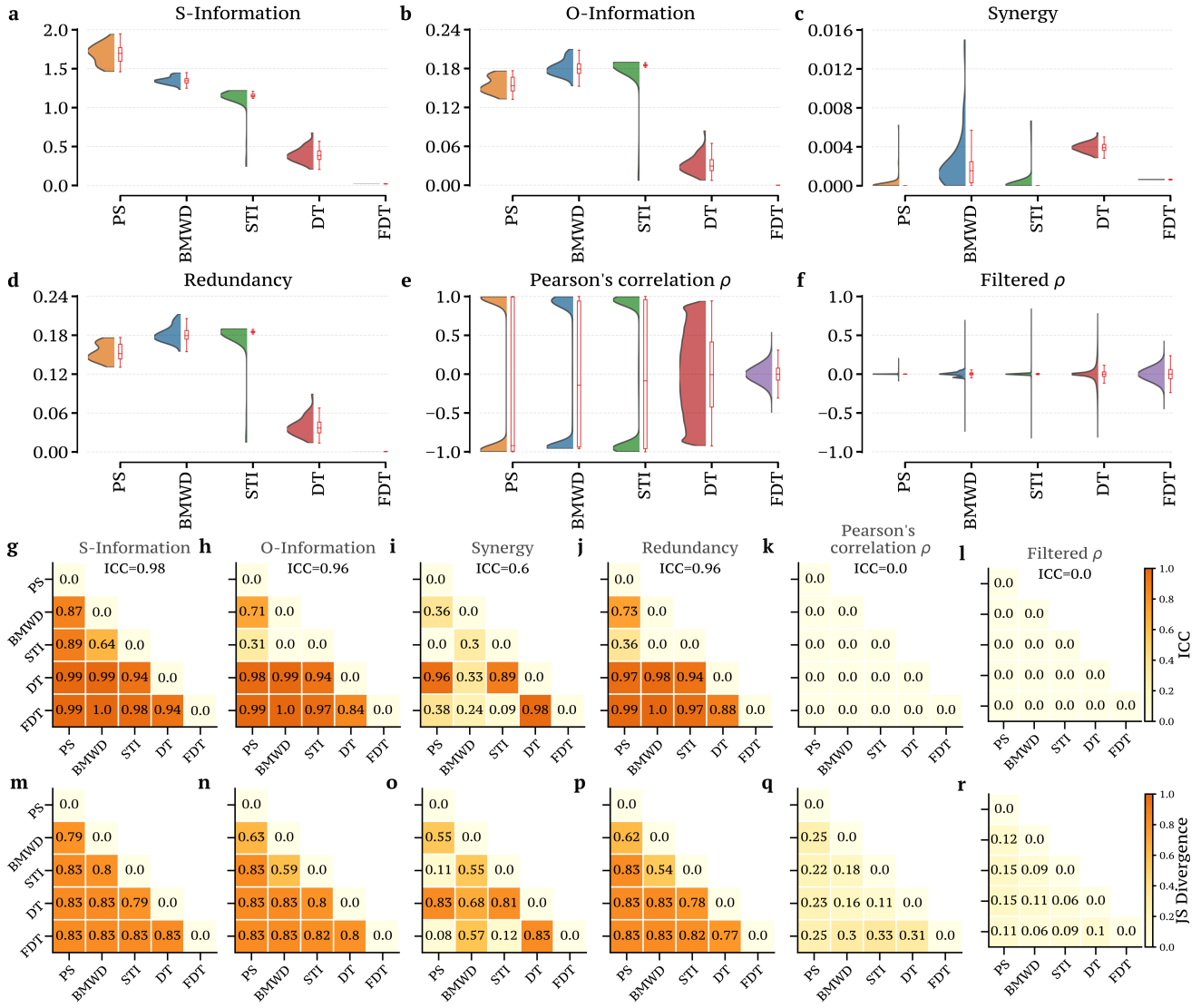


Figure S5: Comparison between approaches for distinguishing the CML regimes. (a-f) For the five dynamical regimes generated by the diffusively coupled chaotic maps, we report the violin plots showing the distribution of “static” higher-order measures [9], and “static” pairwise measures, namely, the Pearson’s correlation coefficient ρ and filtered ρ obtained by considering the approach based on random matrix theory [11]. Remarkably, only higher-order measures are able to separate the five dynamical regimes. (g-l) We report the *ICC* values associated with each metric, either computed considering the five distributions or between all the possible pairs, thus demonstrating that higher-order measures outperform statistics based on pairwise correlations. (m-r) We repeat the same analysis but considering the Jensen-Shannon (JS) divergence to measure distances between distributions, leading to the same conclusions of the *ICC* approach.

S4 Impact of different null models

S4.1 CML synthetic multivariate time series

After having demonstrated that standard metrics to assess two-body similarity of time series, such as RSS, pearson correlation, or more refined approaches based on random matrix theory [11], fail to distinguish the CML dynamical regimes, we now shift the focus to investigating the impact of alternative null models [17, 18, 19]. Indeed, the null reported in Figs. 2-3 of the main text — obtained by independently shuffling the time series — might be in principle too simplistic to detect regime-specific features of the co-fluctuations in the CML case. This is because the empirical signal of the co-fluctuations in each dynamical regime is compared to products of node-level signals at different times and for different regimes. As a consequence, we test the global behaviour of our two higher-order indicators when considering two alternative null models, namely, the (*i*) block null model, and the (*ii*) phase randomization null model. The first null model, hereafter denoted as *block null model*, is constructed such that the shuffling of each dynamical regimes of the CML is performed separately for each region (i.e. the blocks consisting of 240 time points). In this way, we are ensuring that the dynamical regimes are not mixed during the reshuffling, and we can therefore detect regime-specific features of the co-fluctuations.

The second null model, hereafter denoted as *phase randomization null model*, is a conventional approach [17] to generate surrogate time series preserving the empirical power spectra, while randomizing the temporal dependencies. More specifically, such time series are generated by transforming the CML time series to the frequency domain via Fourier transform, shuffling the phase coefficients, and then taking the inverse transform to the time domain [19].

We first aim at replicating the panels of Fig. 2(a,c) of the main text when considering the two alternative null models. In particular, Figure S6 summarizes the results of our higher-order approach when applied to the two surrogate multivariate series. We find that the distributions of hyper-coherence in the block null model become less distinguishable from each other, while keeping certain regime-specific features of the co-fluctuations. Furthermore, the block null model does not preserve any more the ranking between order (i.e. the PS regime) and disorder (i.e. the Spatiotemporal Chaos), see Fig. S6(a). In addition, the distributions of hyper-complexity in the block null model are mostly identical to each other for the five blocks, so that it is clear that there are some intrinsic topological properties that are only present in the CML multivariate time series [see Fig. S6(b)]. When considering the phase randomization null model, we find a flat behaviour for both the hyper-coherence and hyper-complexity distributions, see Fig. S6(c-d).

As done in previous sections, to quantitatively test the ability to distinguish the different CML dynamical states in the null models, we rely again on the ICC values, which are either computed considering the five distributions or between all the possible pairs of regimes. We report in Figure S7 the distributions of hyper-coherence and hyper-complexity for the actual CML time series and for all the different surrogates time series.

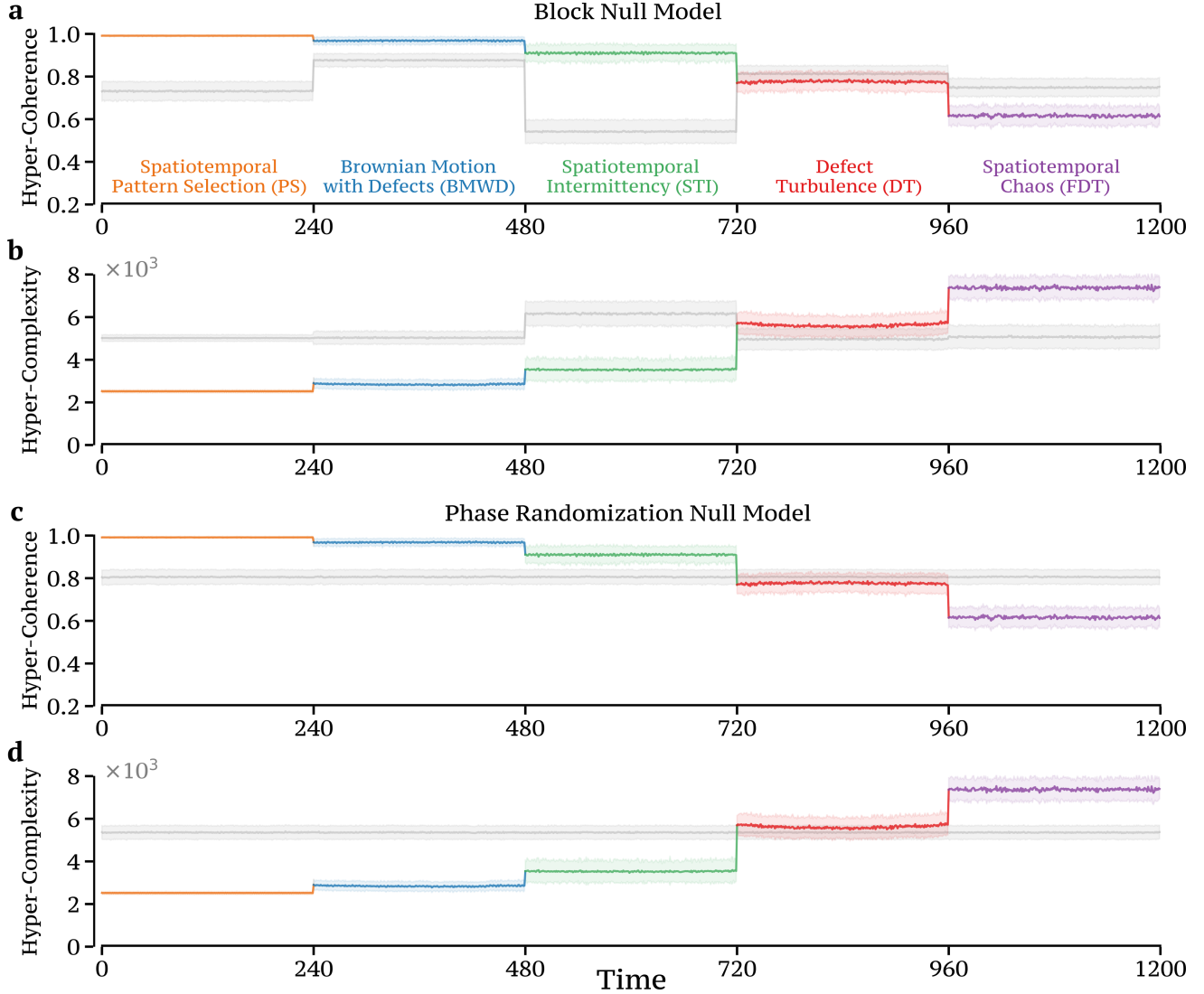


Figure S6: Global behaviour of our higher-order indicators for two alternative null models. (a-b) We report the behaviour of the two higher-order indicators, as in Fig. 2 of the main text, respectively computed for the original CML and for the surrogate time series generated by the block null model, which shuffles independently each block of 240 time points. Remarkably, the resulting blocks of hyper-coherence in this null model become less distinguishable from each other, while keeping certain regime-specific features of the co-fluctuations. However, the ranking from ordered to disordered states is now lost. In addition, the blocks of hyper-complexity cannot be separated in the block null model, somehow supporting the intuition that this topological-based measure is more fine-grained than the hyper-coherence. (c-d) The same analyses are repeated when considering the phase randomization null model, which preserves the power spectra of the CML time series.

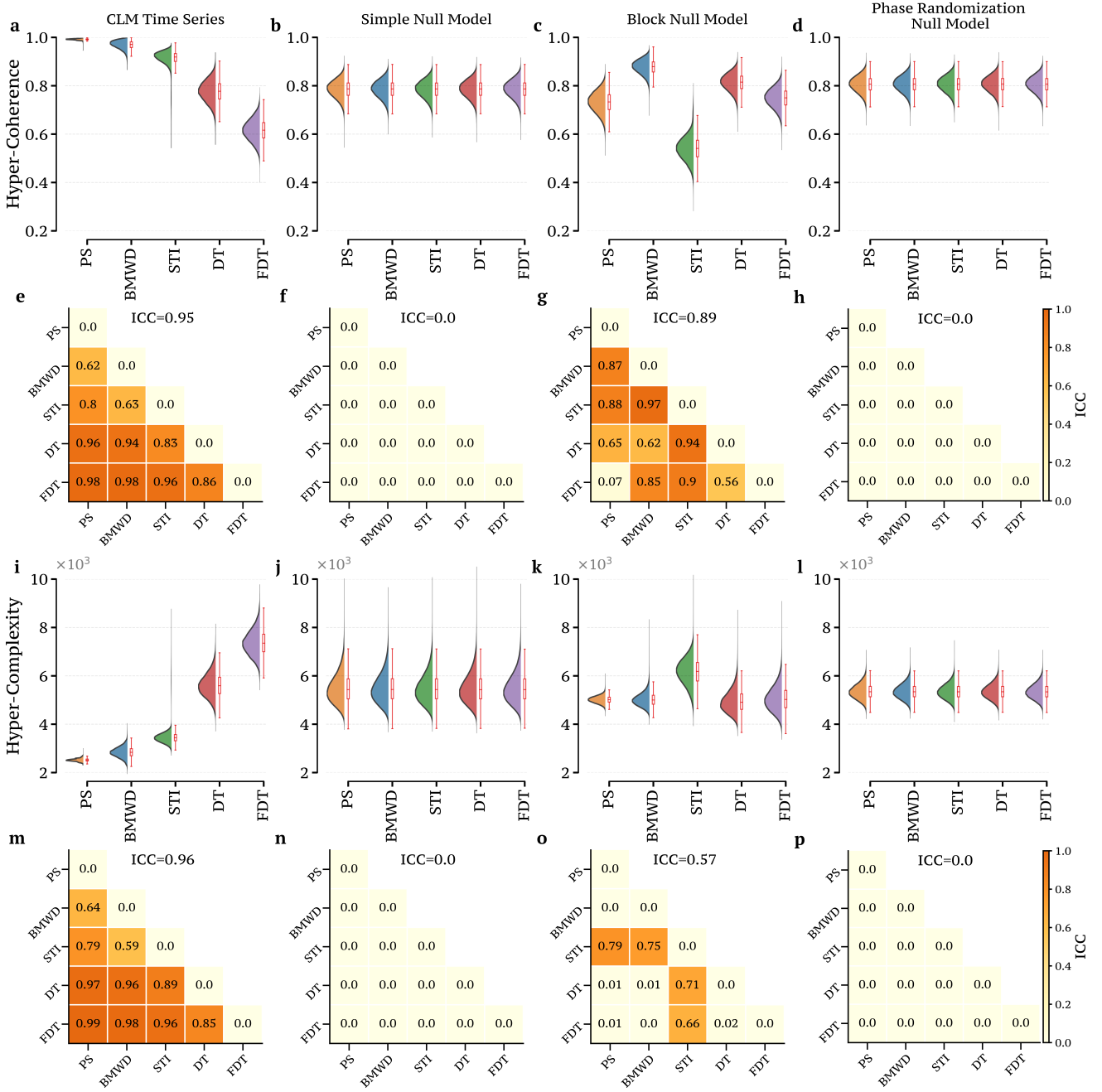


Figure S7: Comparison of null models in Coupled Map Lattice. **(a-d)** We report the distribution of hyper-coherence for the classical CML time series and for the three null models considered in this work, namely, the simple null model considered in the main text, the block null model, and the phase randomization null model. **(e-h)** Both the global and pairwise analysis of the ICC metric reveal that only the block null model is able to partly separate the CML regimes, hence keeping certain regime-specific features of the co-fluctuations, while breaking the order-disorder gradient present in the real hyper-coherence distributions. **(i-l)** When repeating the analyses of panels (a-d) for the distribution of hyper-complexity, we find that the distributions of hyper-complexity in the null models are mostly identical to each other for the five blocks, so that it is clear that there are some intrinsic topological properties that are only present in the CML multivariate time series. **(m-p)** Global and pairwise analysis of the ICC metric provide a quantitative way of assessing the similarities between each regimes in the different null models.

S4.2 Block null model in financial time series

Here, we assess whether the results of hyper-coherence of the financial time series presented in the main text can be trivially obtained by analysing block null models which account for different global trends, including upwards and downwards ones. As a matter of fact, in the considered time span of 21 years (2000-2021) the market experienced different global trends. Therefore, when considering a simple null model, as the one described in the main text, which independently reshuffles each stock price in the whole window, we might neglect the importance of different financial trends. In order to assess this potential confound, we consider three different block null models with respectively 3, 6, and 9 temporal blocks, and test whether the findings on financial time series in the main text could not be simply deduced from more sophisticated null models. The blocks are selected in order to capture the major financial trends of the last 21 years and to consider crises as midpoints of equally spaced time windows.

In Figure S8 we report the distributions of hyper-coherence for the financial dataset along with the four null models obtained by independently reshuffling the real-world multivariate time series over the whole time window of 21 years, or restricting the shuffling over 3, 6, or 9 temporal blocks, respectively. It is interesting to notice that null models with finer information about the global financial trends seem to increasingly approximate the distribution of hyper-coherence of the empirical dataset, despite some notable differences are present even in the finer model consisting of 9 temporal blocks. For example, the distribution of the 9 blocks null model is almost 4-modal, while it is bi-modal in the empirical case, and the two distribution are statistically different, i.e. $p < 10^{-10}$ after the Kolmogorov-Smirnov test. Finally, for the sake of completeness, we report the list of periods considered for the block null models in Figure S8(b).

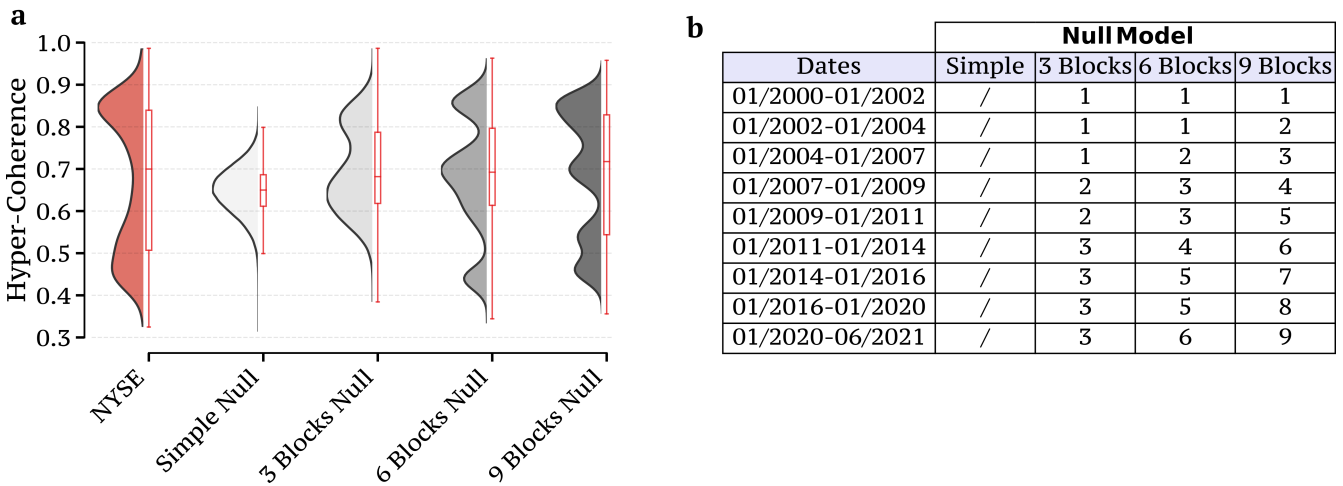


Figure S8: **Distribution of hyper-coherence for different block null models.** (a) Violin plots showing the distribution of hyper-coherence for the financial prices of 119 assets in NYSE spanning a period from 01/2000 to 06/2021. We also report the corresponding null models obtained when independently reshuffling the empirical time series over the whole time window of 21 years (i.e. Simple Null), or restricting the shuffling over 3, 6, or 9 blocks, respectively. Even when considering the null model obtained with 9 blocks (dark grey curve), the hyper-coherence distribution is distinct from the one obtained for the empirical multivariate time series (red curve). (b) We report the periods considered for the various null models, which include finer information about the global financial trends. For instance, the 3 block null model spans three different periods, namely, 01/2000 – 01/2007, 01/2007 – 01/2011, and 01/2011 – 06/2021.

S4.3 Null model of fMRI time series and Gaussian hypothesis

In this section we show the hyper-coherence distribution obtained when considering a N -dimensional Gaussian multivariate time series, where each of the time series is sampled from a normal distribution $\mathcal{N}(0, 1)$ with zero mean and unit variance.

We report in Figure S9 the violin plots reporting the hyper-coherence distribution computed from resting-state fMRI data, the corresponding null model obtained when independently reshuffling the time series, and from Gaussian multivariate time series. It is interesting to notice how the null model of the resting-state fMRI leads to a hyper-coherence distribution that is statistically equivalent to the one obtained when analysing Gaussian multivariate time series (p -value $< 10^{-10}$ with the Kolmogorov-Smirnov test). This is due to the fact that, even though each BOLD signal is not Gaussian per se, the entire ensemble can be considered as Gaussian. As a result, the simple shuffling procedure destroys all the temporal dependencies and the resulting co-fluctuations of the multivariate signals tend to a Gaussian distribution.

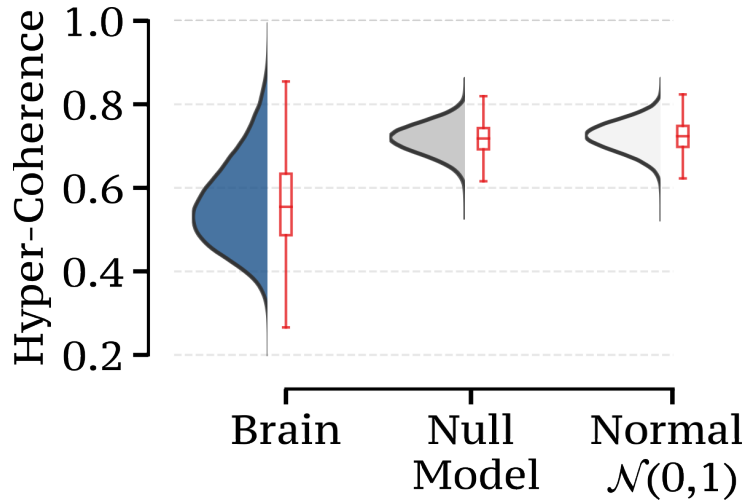


Figure S9: Hyper-coherence distribution computed from resting-state fMRI data and Gaussian multivariate time series. Violin plots showing the distribution of hyper-coherence for the resting-state fMRI data ($N=119$ brain regions), the corresponding null model obtained when independently reshuffling the time series, and for a multivariate time series, where each of the time series is sampled from a normal distribution $\mathcal{N}(0, 1)$. The null model of the resting-state fMRI data leads to a distribution of hyper-coherence that is statistically equivalent to the one obtained when analysing Gaussian multivariate time series (p -value $< 10^{-10}$ with the Kolmogorov-Smirnov test).

S5 Edge-based indicators in real-world systems

In this section we investigate the impact of edge-based statistics in the context of real-world multivariate time series when compared to the higher-order approach presented in the main text. More specifically, we first analyse the RSS distributions for the three types of real-world systems considered in this work. Subsequently, we aim at reproducing some of the results of Fig. 5 of the main paper by relying on metrics derived from RSS or, more in general, from measures based on edge signals. Our final goal is to compare several different group-order representations in the context of the real-world systems considered in this study.

As global analysis, we report in Figure S10 the distributions of RSS for the three real-world datasets. For the sake of comparison, we also plot the null models obtained by independently reshuffling the real-world multivariate time series. We first notice that, in contrast with the results reported in the main text, these distributions are not always statistically distinct from the corresponding null models, as evident when looking at the distributions of the epidemic data (e.g. $p < 0.001$ for Gonorrhea with the Kolmogorov-Smirnov test). Moreover, when examining the RSS distribution of resting-state brain and of financial systems, it is not possible to extract insights on the nature of different temporal dynamics present in the system (e.g. we cannot discriminate crises from periods of financial stability).

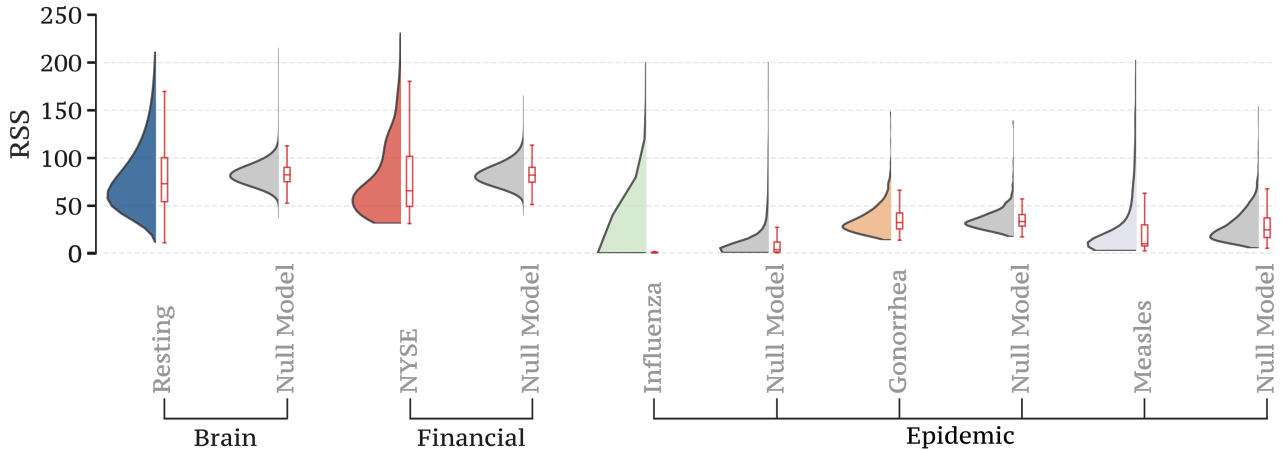


Figure S10: **RSS distribution for the empirical time series.** Violin plots showing the distribution of RSS for the three real-world datasets considered in the main text, namely, resting-state fMRI data ($N=119$ brain regions), financial prices of 119 assets in NYSE in the period 2000-2021, and the US historical data of several infectious diseases at the US state-level ($N=50$). While for the brain and financial systems the empirical RSS distributions are different from the corresponding null models (obtained by independently reshuffling each time series), the RSS distributions for the epidemic time series are very similar to the ones obtained when considering the corresponding null models ($p < 0.001$ for Gonorrhea, with the Kolmogorov-Smirnov test).

Once we established that global edge-wise measures such as RSS provide moderate information on the empirical systems, we now shift the focus on investigating the impact of different group-order representations on a more local level. In particular, we performed several analyses on the empirical time series by projecting the magnitudes of higher- and lower-order approaches on nodal level and compare the overall results. Yet, we remind that any lower-order projection might lead to a moderate/high reduction of the total amount of information and therefore such representations might be potentially misleading if not carefully analysed.

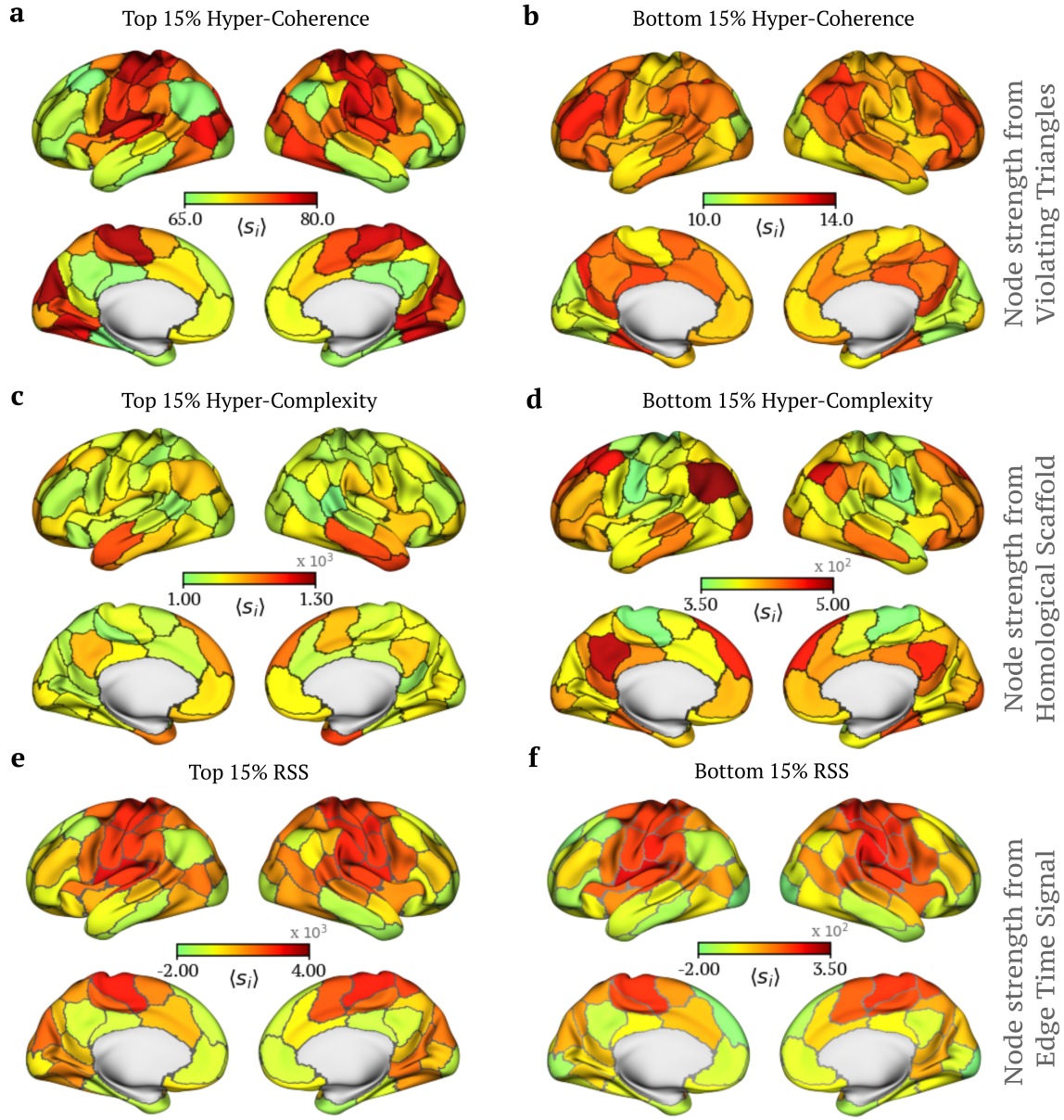


Figure S11: Impact of different group-order representations in brain patterns. Node strength extracted from the violating triangles Δv , homological scaffold, and edge time series can be used to track the importance of group-order structures. **(a-b)** We report the brain map of the nodes involved in higher-order co-fluctuations obtained when isolating the 15% high- and low- coherent frames, respectively. **(c-d)** We report the brain map of the nodes involved in homological scaffold obtained when isolating the 15% high- and low- complexity frames. To compare different group-order representations, we also performed a similar analysis as panels (a-d), yet considering the nodal strength extracted from the edge-wise representation. In particular, **(e-f)** we map onto the cortical surface the nodal strength extracted directly from the 1-order co-fluctuations (i.e. the edge time series), computed from the 15% high- and low-amplitude frames, which have been selected using the RSS statistics. Despite losing part of the information by projecting each group-order representation on a nodal level, we observe that the brain patterns uncovered by top- and low- peaks of the higher-order approach provide different brain configurations compared to edge-wise representation, with the only exception being the top hyper-coherence frames (see Fig. S12 for all the correlations of activity patterns). Results are averaged over all 100 HCP subjects and scans.

Figure S11 summarizes the results of our comparisons for the brain data. Here, we mapped the node strength extracted from the violating triangles Δ_v , the homological scaffold, and the edges time series onto the cortical surface and found various patterns of co-fluctuations. In particular, we first observe that brain patterns uncovered by the 15% top hyper-coherent frames provide quite similar brain configurations as the ones constructed from both top- and bottom-RSS edge-wise representations. By contrast, all the other representations based on higher-order measures provide different brain activity patterns, with the nodal strength of the homological scaffold from the 15% bottom hyper-complexity frames mostly encompassing the Default Mode Network (DMN), see Fig. S11(d).

Yet, the analyses presented so far provide only a qualitative comparison between the approaches. We therefore quantitatively investigate the spatial patterns identified on both resting-state brain data and financial systems by the various methods and compare them considering nodal projections.

For clarity, we first provide in Table S1 a summary description of each method, while we report in Figure S12 the matrices encoding all the possible Pearson's correlations between the various spatial distributions for both the brain data and financial data. In particular, by analysing Figure S12(a), we confirm in a quantitative way that the spatial patterns uncovered by the 15% top-peaks of the higher-order approach using the hyper-coherence (i.e. $\uparrow \Delta_v$) provide brain patterns which are very similar to the ones constructed from both top- and bottom-RSS edge-wise representations. Therefore, at least in brain resting data, such representation might lead to similar results as the one obtained using edges. By contrast, the other higher-order approaches provide patterns that are not entirely deducible from an edge-wise approach and, as such, they might provide new insights into brain dynamics. However, when analysing the same correlation matrix for financial systems [Figure S12(b)], we surprisingly find a rather different picture. In this case, the spatial pattern of the top 15% hyper-coherent frames (i.e. $\uparrow \Delta_v$) is very dissimilar from all those obtained using edge approaches (i.e. $\rho \approx 0$), while the other higher-order approaches still provide patterns that are not captured by any edge-wise approach. This confirms

Method	Description
$\uparrow \Delta_v$ ($\downarrow \Delta_v$)	The top (bottom) 15% of hyper-coherent frames are selected using the hyper-coherence indicator. For only those frames, we compute the average spatial distributions by projecting the list of violating triangles Δ_v on a nodal level.
$\uparrow HC$ ($\downarrow HC$)	The top (bottom) 15% of the hyper-complexity frames are selected using the hyper-complexity indicator. For only those frames, we compute the average nodal strength from the homological scaffold, which is obtained from the persistent homology generators of H_1 [20].
$\uparrow eFC$ ($\downarrow eFC$)	The top (bottom) 15% of the amplitude frames are selected using the RSS measure. From those frames, we then compute the edge functional connectivity matrix [21] and report the nodal strength obtained from such a matrix.
$\uparrow eTS$ ($\downarrow eTS$)	The top (bottom) 15% of the amplitude frames are selected using the RSS measure. For those frames, we then compute the average activity of the 1-order co-fluctuation (i.e. the edge time series) and report the nodal strength.
$\uparrow nodal$ ($\downarrow nodal$)	The top (bottom) 15% of the frames are selected using a RSS-like statistic but computed on the raw signal. For those frames, we then compute the average activity pattern to obtain nodal maps.

Table S1: **Summary of the different approaches.** We provide a short description of the methods considered in this study to construct spatial maps from multivariate time series. We remind also that Δ_v and HC are higher-order measures, eFC and eTS are edge-wise statistics, while $nodal$ corresponds to spatial measures based on the original nodal signal.

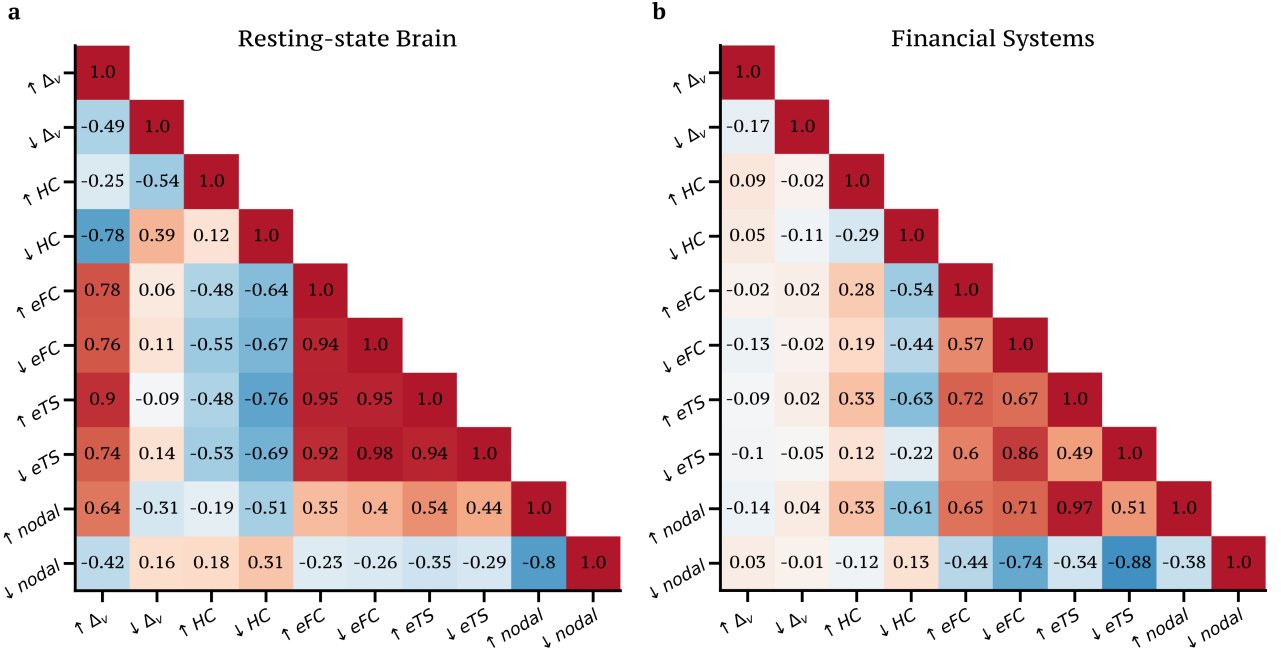


Figure S12: Correlations between group-order representations of brain and financial patterns. We report the Pearson’s correlation coefficient ρ obtained when comparing the nodal projections for (a) brain and (b) financial systems. Here we have that Δ_v and HC are higher-order measures, eFC and eTS are edge-wise statistics, while *nodal* corresponds to measures based on the nodal signal. \uparrow (\downarrow) correspond to the 15% top- (respectively bottom-) peaks of the selected measures. For the sake of clarity, in Table S1 we reported a short description of the methods. Interestingly, while the spatial patterns uncover by the 15% top-peaks of the higher-order approach using the hyper-coherence (i.e. $\uparrow \Delta_v$) provide brain patterns very similar to the ones constructed from both top- and bottom-RSS edge-wise representations, all the other three higher-order approaches provide patterns that are not entirely deducible from an edge-wise approach. However, in financial systems we have an opposite view, so that the patterns obtained from the top 15% hyper-coherent frames (i.e. $\uparrow \Delta_v$) is now very dissimilar from all the ones obtained using edge approaches (i.e. $\rho \approx 0$).

our intuition that various real-world systems might be affected, in varied ways, by group-interactions at different instants in time.

Finally, by analysing the historical data of epidemic outbreaks in the US, we show that the temporal evolution of the RSS measure cannot be effectively used to classify different infectious diseases. Indeed, with a Random Forest classifier we obtain an accuracy level of around 67% using a 10-fold cross-validation setting repeated 50 times. This is quite lower than the result reported in Section S7.1, where instead the classification is based on the higher-order indicators.

S6 Local higher-order indicators in real-world systems

S6.1 Role of thresholds in brain maps

In the main text, we have shown that the nodal strength obtained when projecting either the magnitudes of the violating triangles Δ_v , or the homological scaffold on a nodal level might provide interesting information about the group co-fluctuations of certain brain regions. In particular, since our goal was to characterize the higher-order states with the largest level of synchronization, we isolated only the 15% high-coherent (resp. low-complex) frames. Yet, in principle, a different percentage of selected peaks might translate into a distinct brain activation maps. As a consequence, in Fig. S13 we report the same brain maps as shown in the main text, yet we vary the percentage of peaks selected.

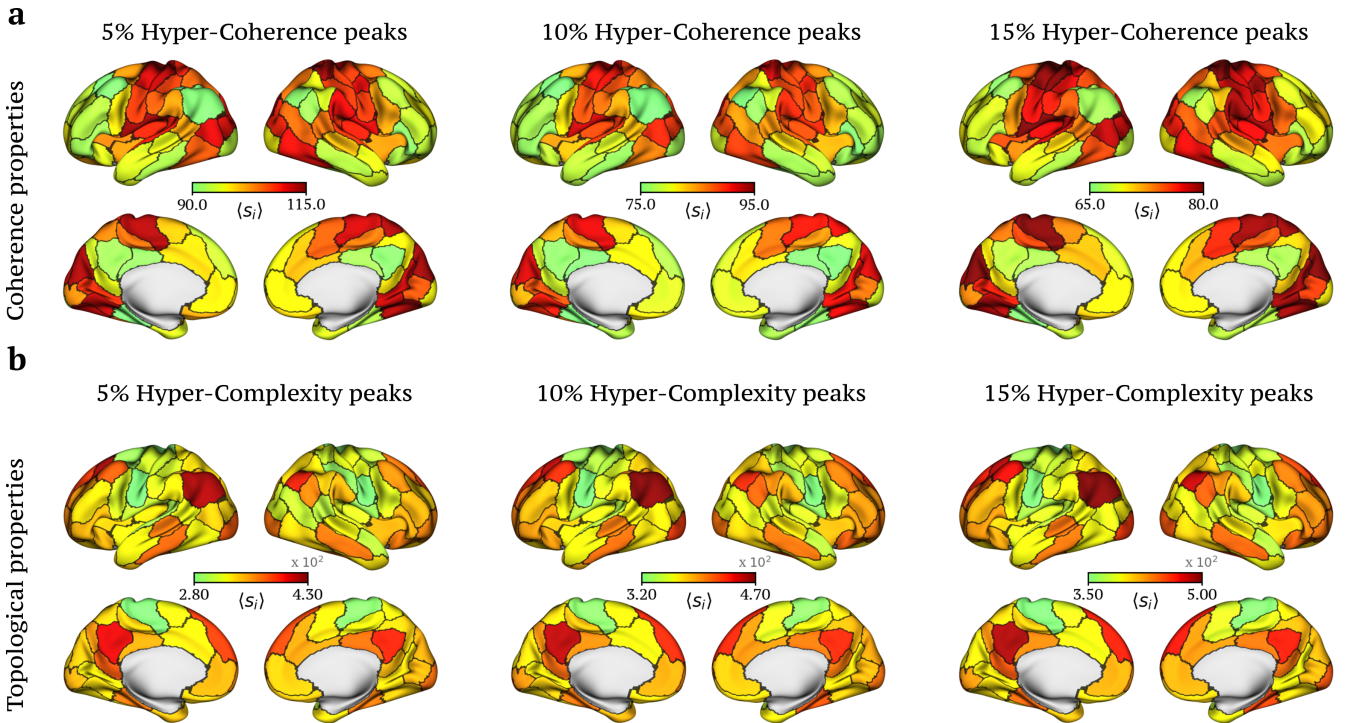


Figure S13: Brain maps with different percentage of peaks. The nodal strength extracted from either the violating triangles Δ_v or the homological scaffold can be used to track the importance of higher-order structures in time. **(a)** Brain maps of the nodes involved in higher-order co-fluctuations obtained when respectively isolating the 5, 10, 15% high-coherent frames, which are those associated with a more synchronized dynamical phase. Interestingly, brain maps are highly consistent across different values of threshold. From a topological perspective, the nodal strength extracted from the homological scaffold provides information about 1D loops in the space of co-fluctuations. **(b)** Brain maps obtained when respectively selecting the 5, 10, 15% low hyper-complexity frames reveal the consistent activation of the Default Mode Network. Indeed, also in this case, the brain maps are mostly the same for different threshold values.

S6.2 Higher-order indicators in the brain's functional networks

In this section, we consider the local higher-order indicators introduced in the main text to analyze the brain at the level of the 7 functional Yeo networks [22] and subcortical regions. In particular, we project the normalized magnitude of the violating triangles Δ_v extracted from the 15% top hyper-coherent frames and of the homological scaffold extracted from the 15% low hyper-complexity frames at the nodal and edge

level. This provides us with information about the most prominent functional networks when isolating a certain percentage of frames both at the level of nodes and edges. Figure S14(a) reports the mean hyper-coherence within- and between- the 7 functional Networks plus subcortical regions, namely, the Visual (VIS), SomatoMotor (SM), Dorsal-Attention (DA), Ventral-Attention (VA), Limbic (L), FrontoParietal (FP), Default Mode Network (DMN), and subcortical regions (SUBC). While the top boxplots (also shown in the main text) report the mean hyper-coherence within the 7 functional Networks, the entries of the matrix encode the mean hyper-coherence within- and between- the 7 functional networks and subcortical regions obtained when projecting Δ_v at the level of their interacting edges. Notably, hyper-coherent interactions (i.e. the triangles) are mainly overrepresented in sensorimotor areas. By contrast, when analysing the mean persistence of 1D holes considering the homological scaffold, we find that such loops are highly concentrated around the DMN and FP areas, as shown in Fig. S14(b), mirroring the importance of such areas in integrating high and low-order systems.

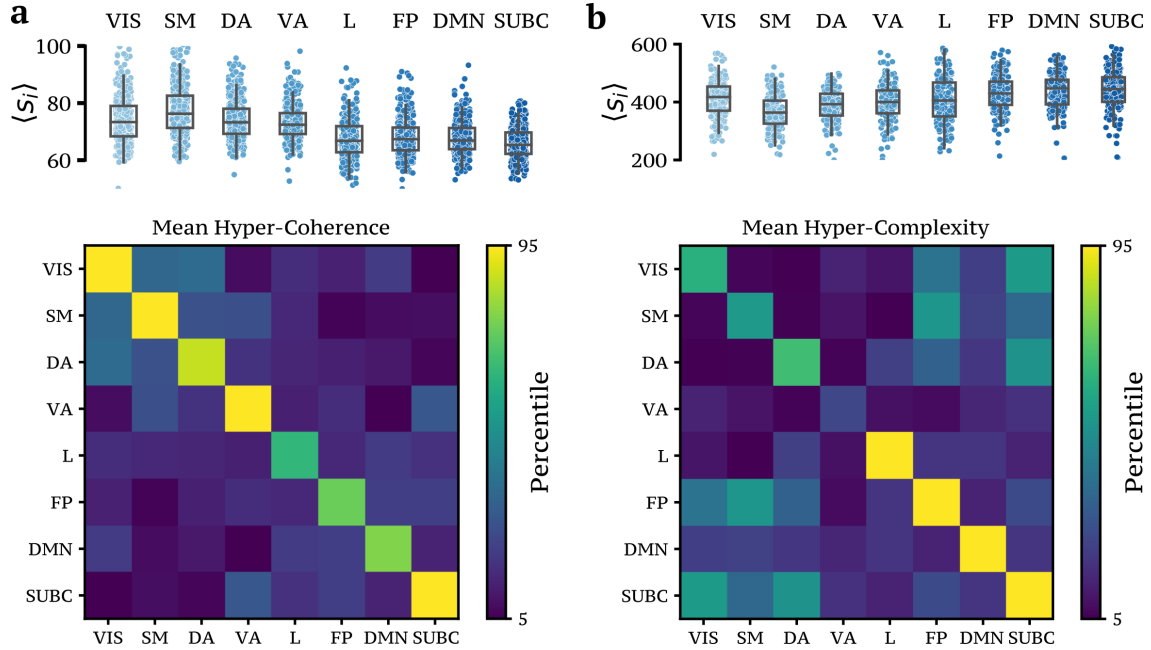


Figure S14: Mean within- and between higher-order indicators in the seven functional networks. For the two local higher-order indicators considered in the main text, namely, **(a)** the list of violating triangles Δ_v and **(b)** the homological scaffold, we report the mean nodal strength and average edge strength within- and between- the 7 functional Networks and subcortical regions, namely, the Visual (VIS), SomatoMotor (SM), Dorsal-Attention (DA), Ventral-Attention (VA), Limbic (L), FrontoParietal (FP), Default Mode Network (DMN), and subcortical regions (SUBC). When analysing the list of violating triangles Δ_v , we find that activity patterns with emphasized synchronized co-fluctuations mainly reflect sensorimotor areas, whereas the persistence of 1D holes obtained from homological scaffold are situated around the DMN and FP areas.

S7 Additional real-world application: the US historical data of infectious diseases

In this section, by analysing the historical data of epidemic outbreaks in the US, we show that the temporal evolution of the higher-order measures (i.e. hyper-coherence, the three contributions of hyper-complexity, and the average edge violations) can be used to classify different infectious diseases. In particular, a support vector machine (SVM) classifier reports a high accuracy level, i.e. around 85 %, using a 10-fold cross-validation setting repeated 50 times (for a comparison between classifiers see Table S2). To provide a more intuitive representation of this result, we report in Fig. S15 a planar embedding of the historical data of epidemic outbreaks obtained using the t-distributed Stochastic Neighbor Embedding (t-SNE) nonlinear dimensionality reduction method. Note that nonlinear methods, such as t-SNE, allow to preserve the “local” structure in the original high-dimensional space after projection into the low-dimensional space, which is typically not possible with linear methods like Principal Component Analysis (PCA) or Multidimensional Scaling (MDS) [23]. In this space, we observe that diseases of different kinds cluster together to a great extent, somehow reflecting the unique spatiotemporal evolution of the outbreaks, which are indeed captured by the SVM classifier. At the same time, similarities between diseases can be observed. This is the case for sexually transmitted diseases, such as gonorrhea and chlamydia, which are mostly overlapping in the planar embedding. As inset plots, we also report the map at the US-state level obtained when selecting the 15% high-coherent frames and considering the nodal-strength of the violating triangles Δ_v . We find that the spatiotemporal evolution of the outbreaks is different across states and diseases, somehow reflecting the unique “higher-order” characteristics of the disease.

S7.1 Comparison of classifiers for the US historical data

In the previous section, we reported the average accuracy score when considering the Support Vector Machine (SVM) method applied to the classification problem of the US historical data of several infectious diseases at the US state-level.

In particular, we have considered the following set of features for the classification task: hyper-coherence, the three different contributes of hyper-complexity, and the average edge violation. In Table S2, we report the scores of several classifiers obtained when considering a 10-fold cross-validation repeated 50 times with different training-test data partitions. The classifiers considered are: Gaussian naive Bayes (Gaussian NB), SVM using a Gaussian radial basis function as kernel (RBF SVM), Decision Tree, random decision forest (Random Forest), and k-nearest neighbors algorithm (k-NN, with k=5). Remarkably, the RBF SVM method, together with Random Forest, leads the pack with the highest accuracy of 0.85. All the analysis reported were obtained using the scikit-learn 1.0.2 python library.

Classifier	Avg. accuracy	F1 weighted score
Gaussian NB	0.47	0.43
RBF SVM	0.85	0.85
Decision Tree	0.81	0.81
Random Forest	0.85	0.85
k-NN	0.83	0.83

Table S2: **Comparison of classifier scores.** We report the average accuracy and F1 weighted scores for the classification of the US historical data of several infectious diseases at the US state-level. We consider hyper-coherence, avg. edge violations, and the three different contributes of hyper-complexity as features for our classification task. The classifiers considered are: Gaussian naive Bayes (Gaussian NB), SVM using a Gaussian radial basis function as kernel (RBF SVM), Decision Tree, random decision forest (Random Forest), and k-nearest neighbors algorithm (k-NN, with k=5).

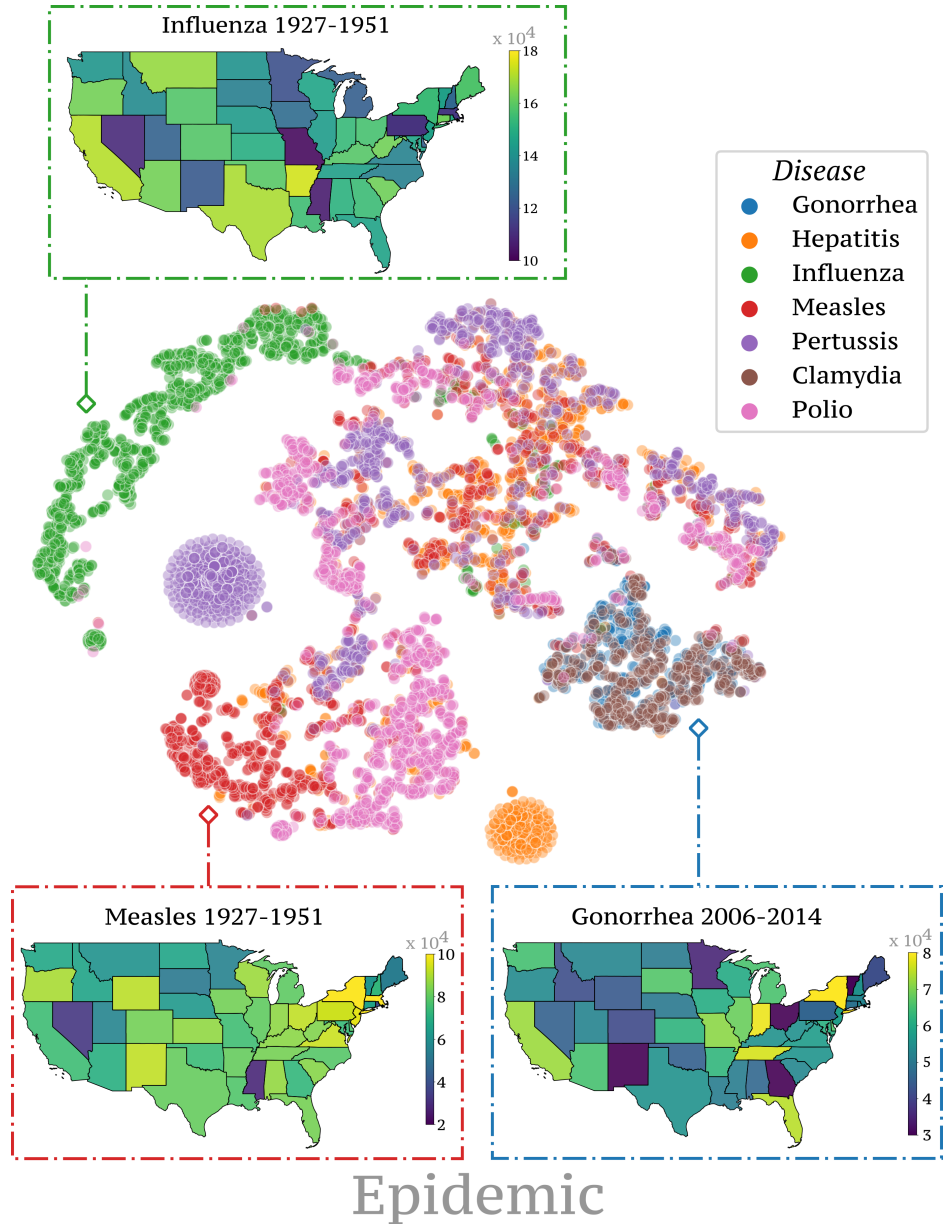


Figure S15: Planar embedding of the historical data of US epidemic outbreaks considering higher-order indicators. We report a planar embedding of the historical data of epidemic outbreaks obtained through t-SNE nonlinear dimensionality reduction when considering as features the higher-order indicators, such as hyper-coherence, the three contributes of hyper-complexity, and the average edge violation (see Method for definition). As inset plots, we report the nodal strength of the violating triangles Δ_v at the US-state level when selecting the 15% high-coherent frames. Remarkably, the spatiotemporal evolution of the outbreaks is different across states and diseases, somehow reflecting the unique “higher-order” characteristics of each disease.

S8 Impact of 3D-cavities in CML

In this section we briefly investigate the presence of 3D-cavities (i.e. the generators of the homology group H_2) when including in the analysis all the interactions up to 4-body interactions. Indeed, in the main text, we mainly focused on analyzing 1D cycles (i.e. the generators of the homology group H_1) of the simplicial filtration $\mathbb{F}(\mathcal{K}^t)$ that we generate at each time t , while we explicitly did not consider 3D-cavities. This is because we limited our analysis up to 3-body interactions (i.e. up to triangles), and 3D-cavities do not add meaningful information. As a matter of fact, if only 3-body interactions are present, then all the 3D-cavities have an infinite persistence due to the absence of 4-body interactions that close cavities. In other words, without 4-body interactions, 3D-cavities will have a birth in the filtration but not a death. Nevertheless, the presence of cavities in the simplicial filtration $\mathbb{F}(\mathcal{K}^t)$ might add important information when characterizing the higher-order structure of a multivariate time series, as shown when analysing the human connectome data [24].

Figure S16 reports the persistence diagrams for the homology groups H_1 , H_2 obtained in the context of Coupled Map Lattices with $N = 50$ nodes when extending our framework to 4-body interactions. Remarkably, we find that the persistence diagram for H_2 is diverse for the five dynamical regimes and, as a result, it might be used together with H_1 to further differentiate the CML dynamical regimes.

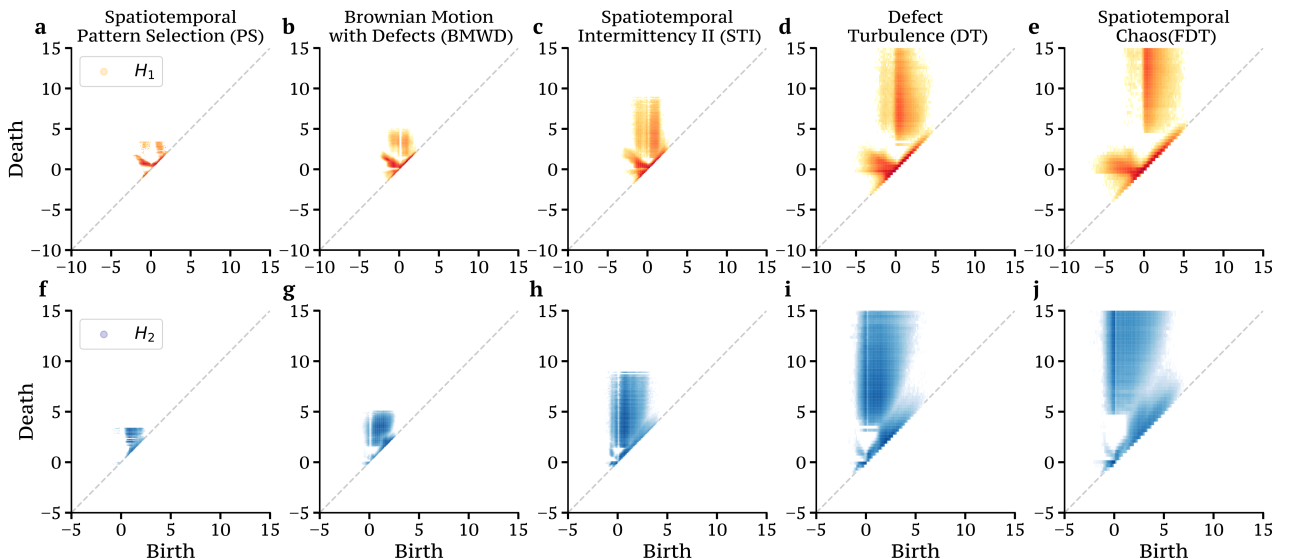


Figure S16: 2D histograms for the H_1 and H_2 generators in Coupled Map Lattices. We report, for each dynamical state of the Coupled Map Lattice with $N = 50$, the persistence diagram for the homology groups H_1 and H_2 . Interestingly, the H_2 persistence diagram is different between the CML dynamical states and, as a result, it might help to further differentiate the five dynamical states when considered in synergy with H_1 . Results are obtained considering 10 independent realization and 240 time points for each block in analogy with the results reported in the main text. The dynamical states are: Pattern Selection (PS) at $\varepsilon = 0.12$, Brownian motion with Defects (BMWD) at $\varepsilon = 0.08$, Spatiotemporal Intermittency II (STI) at $\varepsilon = 0.3$, Defect Turbulence (DT) at $\varepsilon = 0.068$, and Fully Developed Turbulence (FDT) at $\varepsilon = 0.05$, for which a transient of 10^5 time points has been removed.

S9 Effect of noisy fluctuations in brain data

As mentioned in the main text, one of the limitations of our higher-order approach working on single-frame timescales is that it might be affected by noisy fluctuations in the time series, as many of other existing methods [25, 26, 7]. However, in practice, this problem can be smoothed out by analyzing the statistics of multiple time frames. In this section we confirm that, even in presence of noisy fluctuations in brain data (i.e., head movement), the resulting spatial distribution of the hyper-coherence appear to be robust and stable. More precisely, similarly to Ref. [27], we considered frames (i.e. fMRI volumes) affected by head motion if the relative Root Mean Square (RMS) between frames was greater than 0.2, i.e. $RMS > 0.2$.

Figure S17 reports the nodal spatial distributions obtained from the violating triangles Δ_v using the top- and bottom 15% hyper-coherent frames when analysing the fMRI resting-state data in presence and absence of fMRI volumes containing high head motion. Notably, we obtain a Pearson's correlation coefficient $\rho \approx 0.999$ when comparing the resulting brain maps in presence and absence of fMRI volumes affected by head motion.

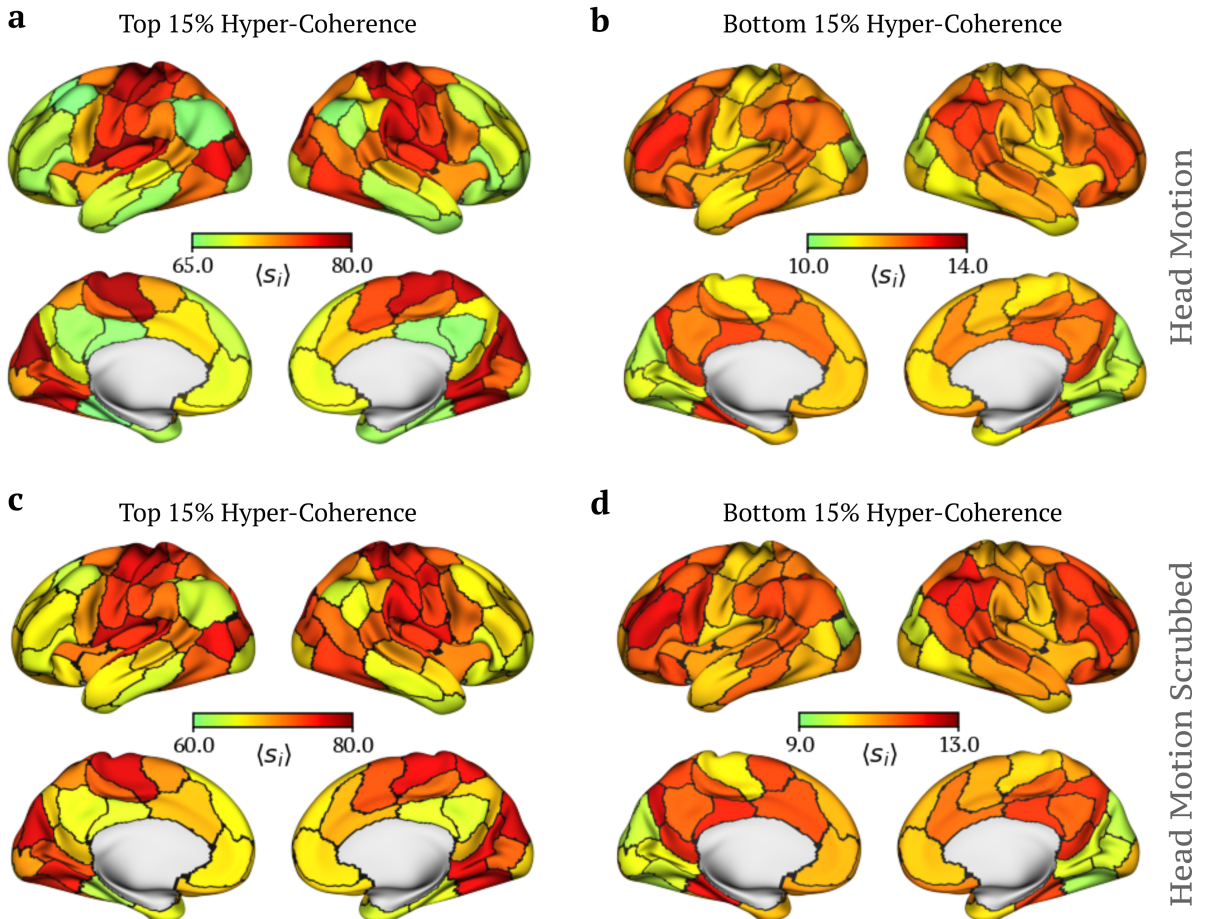


Figure S17: Effect of head motion in brain maps. We report the nodal spatial distributions obtained from the violating triangles Δ_v using the top- and bottom 15% hyper-coherent frames when analysing the fMRI resting-state data in **(a-b)** presence and **(c-d)** absence of fMRI volumes containing noisy fluctuations (head motion). When comparing the resulting brain maps we obtain a Pearson's correlation coefficient of $\rho \approx 0.999$.

References

- [1] Carriere, M., Cuturi, M. & Oudot, S. Sliced wasserstein kernel for persistence diagrams. In *International conference on machine learning*, 664–673 (PMLR, 2017).
- [2] Bevers, M. & Flather, C. H. Numerically Exploring Habitat Fragmentation Effects on Populations Using Cell-Based Coupled Map Lattices. *Theoretical Population Biology* **55**, 61–76 (1999).
- [3] Hilgers, A. & Beck, C. Turbulent Behavior of Stock Exchange Indices and Foreign Currency Exchange Rates. *International Journal of Bifurcation and Chaos* **07**, 1855–1859 (1997).
- [4] Huang, W. & Chen, Z. Heterogeneous agents in multi-markets: A coupled map lattices approach. *Mathematics and Computers in Simulation* **108**, 3–15 (2015).
- [5] Kaneko, K. Pattern dynamics in spatiotemporal chaos: Pattern selection, diffusion of defect and pattern competition intermittency. *Physica D: Nonlinear Phenomena* **34**, 1–41 (1989).
- [6] Kaneko, K. Overview of coupled map lattices. *Chaos: An Interdisciplinary Journal of Nonlinear Science* **2**, 279–282 (1992).
- [7] Esfahlani, F. Z. *et al.* High-amplitude cofluctuations in cortical activity drive functional connectivity. *Proceedings of the National Academy of Sciences* **117**, 28393–28401 (2020).
- [8] Pope, M., Fukushima, M., Betzel, R. F. & Sporns, O. Modular origins of high-amplitude cofluctuations in fine-scale functional connectivity dynamics. *Proceedings of the National Academy of Sciences* **118** (2021).
- [9] Rosas, F. E., Mediano, P. A., Gastpar, M. & Jensen, H. J. Quantifying high-order interdependencies via multivariate extensions of the mutual information. *Physical Review E* **100**, 32305 (2019).
- [10] Gatica, M. *et al.* High-Order Interdependencies in the Aging Brain. *Brain Connectivity* **00**, 1–11 (2021).
- [11] MacMahon, M. & Garlaschelli, D. Community Detection for Correlation Matrices. *Physical Review X* **5**, 021006 (2015).
- [12] Sporns, O. *Networks of the Brain* (MIT press, 2010).
- [13] Shrout, P. E. & Fleiss, J. L. Intraclass correlations: Uses in assessing rater reliability. *Psychological Bulletin* **86**, 420–428 (1979).
- [14] McGraw, K. O. & Wong, S. P. Forming inferences about some intraclass correlation coefficients. *Psychological Methods* **1**, 30–46 (1996).
- [15] Kaneko, K. & Tsuda, I. *Complex Systems: Chaos and beyond: A Constructive Approach with Applications in Life Sciences* (Springer Science & Business Media, Berlin, 2011).
- [16] Núñez, Á. M., Luque, B., Lacasa, L., Gómez, J. P. & Robledo, A. Horizontal visibility graphs generated by type-I intermittency. *Physical Review E* **87**, 052801 (2013).
- [17] Schreiber, T. & Schmitz, A. Surrogate time series. *Physica D: Nonlinear Phenomena* **142**, 346–382 (2000).
- [18] Donges, J. F. *et al.* Unified functional network and nonlinear time series analysis for complex systems science: The pyunicorn package. *Chaos: An Interdisciplinary Journal of Nonlinear Science* **25**, 113101 (2015).

- [19] Váša, F. & Mišić, B. Null models in network neuroscience. *Nature Reviews Neuroscience* 1–12 (2022).
- [20] Petri, G. *et al.* Homological scaffolds of brain functional networks. *Journal of the Royal Society Interface* **10**, 186–198 (2014).
- [21] Faskowitz, J., Esfahlani, F. Z., Jo, Y., Sporns, O. & Betzel, R. F. Edge-centric functional network representations of human cerebral cortex reveal overlapping system-level architecture. *Nature neuroscience* **23**, 1644–1654 (2020).
- [22] Yeo, B. T. *et al.* The organization of the human cerebral cortex estimated by intrinsic functional connectivity. *Journal of neurophysiology* (2011).
- [23] Van der Maaten, L. & Hinton, G. Visualizing data using t-SNE. *Journal of machine learning research* **9** (2008).
- [24] Sizemore, A. E. *et al.* Cliques and cavities in the human connectome. *J Comput Neurosci* **44**, 115–145 (2018).
- [25] Tagliazucchi, E., Balenzuela, P., Fraiman, D. & Chialvo, D. Criticality in Large-Scale Brain fMRI Dynamics Unveiled by a Novel Point Process Analysis. *Frontiers in Physiology* **3** (2012).
- [26] Liu, X. & Duyn, J. H. Time-varying functional network information extracted from brief instances of spontaneous brain activity. *Proceedings of the National Academy of Sciences* **110**, 4392–4397 (2013).
- [27] Jenkinson, M., Bannister, P., Brady, M. & Smith, S. Improved optimization for the robust and accurate linear registration and motion correction of brain images. *NeuroImage* **17**, 825–841 (2002).